ATLAS PUB Note

ATL-SOFT-PUB-2023-001

27th June 2023

Simulation and expected detector performance of fractionally charged particles in ATLAS

The ATLAS Collaboration

Searching for long-lived fractionally charged particles (FCPs) provides a novel opportunity in the exploration for new physics. Many experiments have been carried out to search for evidence of this signature both terrestrially and in space, but no evidence has been observed. This note presents the simulation and detector performance of FCPs in the ATLAS detector for proton-proton collisions at $\sqrt{s}$ = 13 TeV.

1 Introduction

The discovery of the Higgs boson [1, 2] at the Large Hadron Collider (LHC) marked a significant milestone in the field of particle physics. Since then, both the ATLAS and CMS detectors have been operating with increased center-of-mass energy of 13 TeV and a much larger instantaneous luminosity, providing an unprecedented opportunity to reveal new phenomena beyond the Standard Model (SM). No positive signal has been observed to date making more unconventional approaches an appealing avenue to consider. Hunting for long-lived particles, such as fractionally charged particles (FCPs), multi-charged particles (MCPs), magnetic monopoles is well motivated by a range of theoretical models [3–5]

The attraction of FCPs has been inspired by the puzzle of the unit electric charge (e), in that we cannot explain theoretically why the electric charges of all free elementary particles must have to be zero or integer multiples of e. New theories beyond the SM could lead to FCPs with Q = $r \times e$, where r is a fraction or irrational less than one.

Searches for FCPs have been carried out in different ways [6], including fixed-target experiments, collider experiments, cosmic experiments in space and on the earth, and bulk matter experiments. Up to now, there is no evidence for the existence of FCPs.

The CMS experiment searched for FCPs [7, 8] using 5.0 fb^{-1}, 18.8 fb^{-1} and 138 fb^{-1} of pp collision data with $\sqrt{s}$ = 7 TeV, 8 TeV and 13 TeV, respectively, utilizing the dE/dx measurements from the silicon-strip detector and the time-of-flight measurement from the muon system to distinguish the signal from backgrounds. No obvious excess from the SM predictions was found. The analysis using data with $\sqrt{s}$ = 7 TeV and 8 TeV excluded masses below 200 and 480 GeV for $|Q|$ = 1/3 e, 2/3 e respectively. The existence of fractionally charged particles was excluded up to a mass of 636 GeV for a signal of charge $|Q|$ = 2/3 e in the analysis using data with $\sqrt{s}$ = 13 TeV.

FCPs have not yet been searched for in the ATLAS experiment. A future search in ATLAS would also utilize the detector characteristic information such as dE/dx, which can help differentiate the FCPs from SM particles. The performance of dE/dx reconstruction has been studied and verified in a recent search for MCPs [9–11].

In this work, the detector performance of FCPs is studied based on the Monte Carlo (MC) simulation. According to the Bethe-Bloch formula [12], the energy deposition depends quadratically on the charge of particles. The existence of FCPs could be revealed by the different behaviours in the spectrum of measured energy deposition.

This note has been structured as follows. Section 2 introduces the ATLAS detector. Section 3 covers the signal modeling and kinematic distributions at the truth level. Section 4 shows the MC simulation and the detector performance of the FCPs. The last section summarizes the characteristic of FCPs which could possibly benefit future searches with the ATLAS detector.

2 ATLAS detector

The ATLAS detector [13, 14] at the LHC covers nearly the entire solid angle around the collision point[1]. It consists of an inner tracking detector surrounded by a thin superconducting solenoid, electromagnetic and hadronic calorimeters, and a muon spectrometer incorporating three large superconducting toroidal magnets.

The inner-detector system (ID) is immersed in a 2 T axial magnetic field and provides charged-particle tracking in the range $|\eta| < 2.5$. The high-granularity silicon pixel detector covers the vertex region and provides four measurements for most tracks, the first hit normally being in the insertable B-layer [15]. It is followed by the silicon microstrip tracker, which provides eight measurements per track. These silicon detectors are complemented by the transition radiation tracker (TRT), which enables radially extended track reconstruction up to $|\eta| = 2.0$. The TRT also provides electron identification information based on the fraction of hits (typically 30 in total) with an energy deposit above the transition-radiation threshold.

The calorimeter system covers the pseudorapidity range $|\eta| < 4.9$. Within the region $|\eta| < 3.2$, electromagnetic calorimetry is provided by the barrel and endcap high-granularity lead/liquid-argon (LAr) calorimeters, with an additional thin LAr presampler covering $|\eta| < 1.8$ to correct for energy loss in material upstream of the calorimeters. Hadronic calorimetry is provided by steel/scintillator-tile calorimeter, segmented into three-barrel structures within $|\eta| < 1.7$, and two copper/LAr hadronic endcap calorimeter. The solid angle coverage is completed with forward copper/LAr and tungsten/LAr calorimeter modules optimised for electromagnetic and hadronic measurements, respectively.

The muon spectrometer (MS) comprises separate trigger and high-precision tracking chambers measuring the deflection of muons in a magnetic field generated by the superconducting air-core toroid magnets. The field integral $\int \mathrm{Bdl}$ of the toroid magnets ranges from 1.5 to 5.5 Tm in the barrel and 1 to 7.5 Tm in the endcaps. The precision chambers cover the region $|\eta| < 2.7$ with three layers of monitored drift tubes (MDT), complemented by cathode-strip chambers (CSC) in the forward region, where the background is highest. The muon trigger system covers the range $|\eta| < 2.4$ with resistive-plate chambers (RPC) in the barrel, and thin-gap chambers (TGC) in the endcap regions.

[1] Definition of ATLAS coordinate system: the beam direction defines the z-axis and the x-y plane is transverse to the beam direction. The positive x-axis is defined as pointing from the collision point to the center of the LHC ring and the positive y-axis is defined as pointing upwards. The azimuthal angle ϕ is measured around the beam axis, and the polar angle θ is the angle from the beam axis. The pseudorapidity is defined as η = -ln$\tan(\theta/2)$. The transverse momentum p_{T}, the transverse energy E_{T}, and the missing transverse energy $E_{\mathrm{T}}^{\mathrm{miss}}$ are defined in the x-y plane unless stated otherwise.

3 Modeling and kinematic distributions at truth level

3.1 Signal modeling

In the simplified model used in this study, the FCPs are produced through the Drell-Yan process with the mediator being either a Z boson or photon. Events are modeled with proton-proton collisions at $\sqrt{s}$ = 13 TeV.

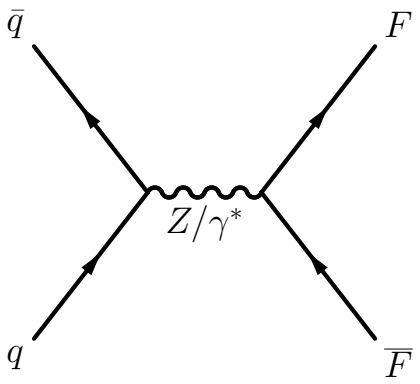

Figure 1: Feynman diagram of $q\bar{q} \rightarrow F\bar{F}$, where "F" refers to an FCP.

The cross-sections of processes under different assumptions of charges and masses are shown in Fig. 2. Those FCPs with higher mass or less charge feature smaller cross-section. Production in the lowest-mass scenario is dominated by on-shell Z production and decay, which results in a charge-independent cross-section. FCPs only participate in the weak and electromagnetic (EM) interactions, meanwhile, their long life-time and high mass implies they will pass through the whole ATLAS detector. So the performance in the detector is like that of muons.

3.2 Characteristic distributions of FCPs at particle level

In order to establish kinematic attributes of FCPs, the velocity (β), pseudorapidity (η),and transverse momentum (p_{T}) of FCPs are studied using MadGraph5_aMC@NLO v2.3.3 [16] with A14 tune and LHAPDF [17] for parton distribution functions and PYTHIA [18] for hadronization. Samples of 30,000 events of $p + p \rightarrow FCP + \overline{FCP}$ have been generated for each mass and charge point at the generator level, i.e. the final stage before going through detector simulation. Those kinematic attributes are found to be correlated to the mass while not sensitive to the charge. FCPs carrying $1/2$ e at different mass points, as representatives, are studied to illustrate the characteristic kinematic attributes.

3.2.1 Velocity

The distributions of β of FCPs at three mass points have been plotted in Fig. 3(a). To further reveal the relation between the velocity and the mass, the average β of FCPs is drawn as a function of the mass

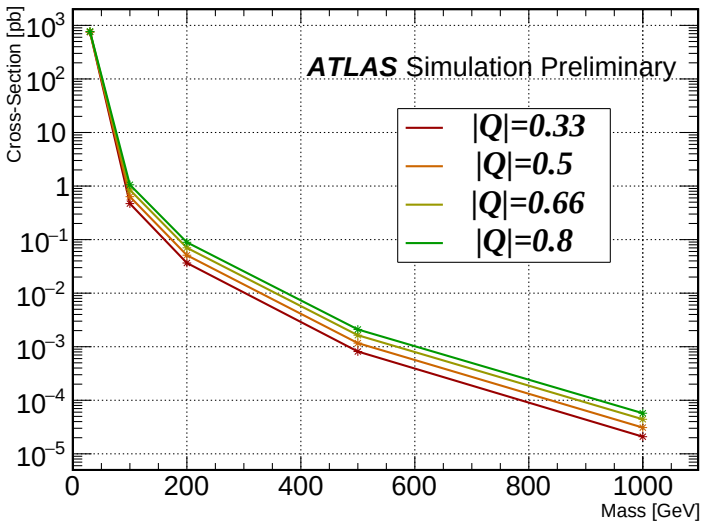

Figure 2: The production cross-sections of FCPs carrying different charges as functions of their mass

indicated in Fig. 3(b). Both figures indicate FCPs with larger mass are slower. The dip in Fig. 3(b) can be explained with the kinematics of the Z-boson decays. The relations between the $\beta\gamma$ and mass of FCPs are similarly illustrated in Fig. 3(c) and Fig. 3(d).

3.2.2 Pseudorapidity

The distributions of $|\eta|$ for FCPs at three typical mass points are plotted in Fig. 4(a) and the correlation between the average of $|\eta|$ and FCP mass is drawn in Fig. 4(b). Both plots indicate FCPs with larger mass are distributed more centrally since the intermediate states of heavy particles are produced approximately at rest. A bump around 45 GeV is due to the Z resonance. Considering the coverage of the ATLAS detector, the distribution of η determines the acceptance of FCPs with a certain mass. In terms of the pixel detector ($|\eta| < 2.5$), the distribution of $|\eta|$ results in a geometrical acceptance of 41% and 85% for 30 GeV and 1000 GeV FCPs, respectively.

3.2.3 Transverse momentum

The distribution of transverse momentum p_{T} for FCPs at three typical mass points are plotted in Fig. 4(c) and the correlation between the average of p_{T} and FCP mass is drawn in Fig. 4(d). Except for the valley around 45 GeV where the Z resonance is, the heavier FCP features higher p_{T} as predicted by the theory, which implies this variable could help distinguish FCPs with different masses.

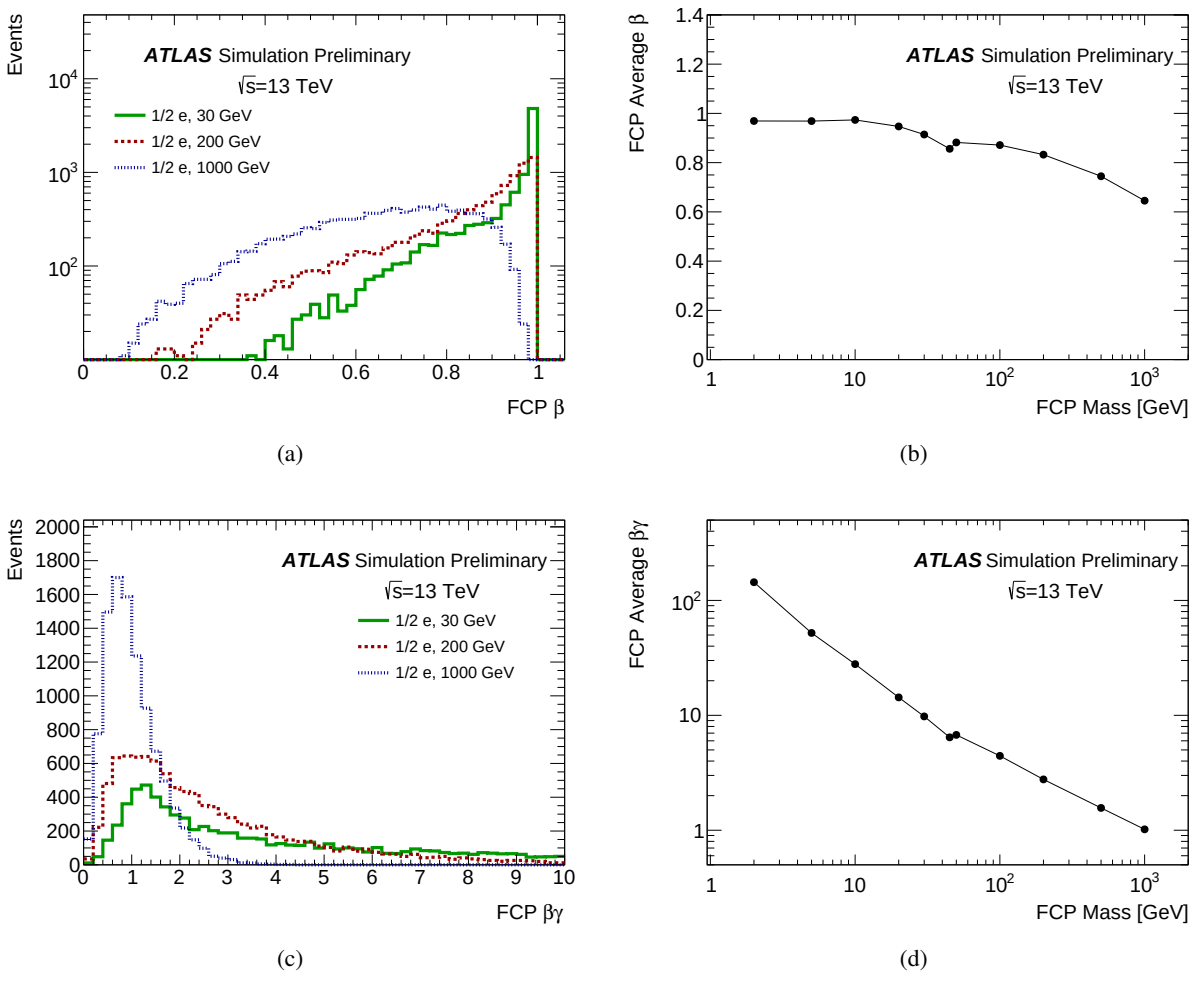

Figure 3: The β of FCPs with different masses is drawn in (a), while the average of the β is drawn as a function of the mass of FCPs in (b). The $\beta\gamma$ of FCPs of different masses are illustrated similarly in (c) and (d).

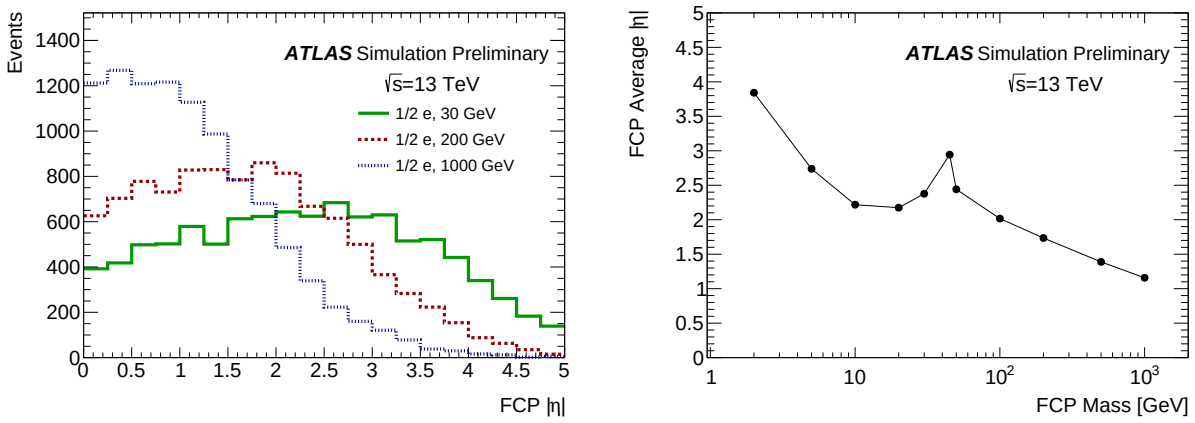

(a) (b)

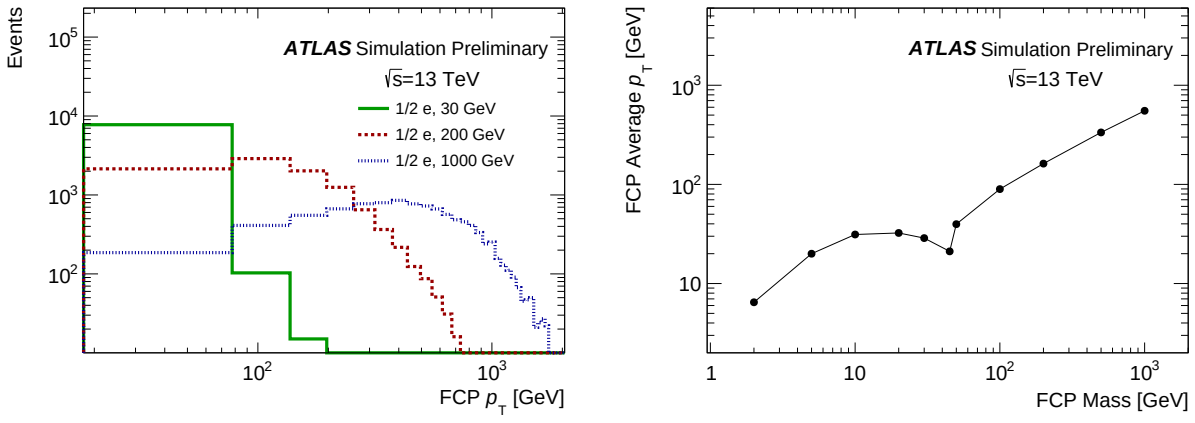

(c) (d)

Figure 4: The $|\eta|$ of FCPs with different masses is drawn in (a), while the average of the $|\eta|$ is drawn as a function of the mass of FCPs in (b). The p_{T} of FCPs is drawn similarly in (c) and (d).

4 Detector simulation and performance

4.1 ATLAS simulation

In the simulation process [19], the charge of an FCP is recognized by the specially encoded pdgId to simulate the energy deposition and the deflection of the track in the magnetic field. Only energy loss of FCP by ionization is included in the detector simulation. The velocity of particles is also considered according to the Bethe-Bloch formula by the full Geant4 [20] simulation. Then the digital signals of various kinds of detectors are simulated according to energy deposition results. The simulation and collision data follow the same reconstruction algorithms. The detector performance, including trigger, energy deposition, reconstructed velocity, etc, are studied in this section.

4.2 FCP reconstruction

Considering the assumption that FCPs are long-lived in the range of the ATLAS detector, FCPs are expected to reach the MS. Thus, it is straightforward to search for FCPs among particles that are reconstructed as muons by the energy deposition and some other sensitive variables. However, the risk in failing to reconstruct an FCP as a muon following conventional algorithms could not be neglected because of the FCP characteristic kinematic attributes and lower energy deposition. A careful study in the reconstruction algorithms has been performed to extend FCP reconstruction efficiency.

Two reconstruction techniques, the standard muon reconstruction [21] and the MuGirl reconstruction [22], are utilized to reconstruct muon-like objects. The first reconstructs so-called combined muons: tracks reconstruction is firstly performed independently in the ID and MS which are then matched with each other [23]. This algorithm assumes particles propagate with the speed of light. The standard muon reconstruction (also standard muon trigger) efficiency starts dropping sharply for $\beta < 0.75$ and goes to 0 at $\beta = 0.4$ since the time-of-flight (TOF) does not match the speed of light assumption. Based on Fig. 3(a), a large part of FCPs especially for mass points 200 GeV and 1000 GeV have β lower than 0.75. So the efficiency for FCPs will not be high. To increase the reconstruction efficiency of particles with heavy mass, the MuGirl algorithm is designed by a previous ATLAS search [24]. The MuGirl reconstruction follows the inside-out approach: it extrapolates ID tracks into MS and then looks for hits in the corresponding detectors. Contrary to the standard muon reconstruction algorithm, MuGirl does not assume particles propagate with the speed of light [25]. Instead, the velocity is additionally fit according to the time information of the hits.

As discussed in section 3.2.1, the velocity of massive FCPs is significantly slower than that of light, thus the MuGirl algorithm benefits the FCP reconstruction in both quality and efficiency. Hence, FCP candidates are firstly collected from the MuGirl objects. Then, event by event, those standard muon objects, which do not match any of MuGirl objects by checking if their ΔR is less than 0.05, are collected as supplementary to maximize the reconstruction efficiency. The ΔR is computed between the tracks of MuGirls or standard muons and truth FCPs as $\sqrt{\Delta\eta^2 + \Delta\phi^2}$.

4.3 Event selection

To study the detector performance of FCPs, the reconstructed muons have to match with the FCPs at the truth level, with a requirement of $\Delta R < 0.05$. For the reconstructed particles, the requirements of η, p_{T} and tracks are applied. As the pixel detector is expected to provide the most accurate identification on

FCPs, the region of interest is $|\eta| < 2.5$ in pseudorapidity space. Besides, the FCPs reconstructed as muons must possess tracks both in ID and MS and p_{T} larger than 27 GeV. Requirements on isolation and impact parameter are not applied for the MC signal samples in this work. And no requirement of detector $\mathrm{d}E/\mathrm{d}x$ is applied in the event selection. For the particles at the generator level, only the requirements of η and p_{T} are necessary and they are the same as the reconstructed objects.

To calculate the efficiency, the denominator is the number of selected FCPs at the generator level. The numerator is the number of real FCPs which could match to reconstructed standard muons or MuGirls. The result of efficiency is shown in Table 1 at different mass and charge points. The low efficiencies for $1/3\ e$, $1/2\ e$ FCPs are due to the detectors not being sensitive to low charges. And the relative high efficiencies for FCPs with high mass benefit from the MuGirl reconstruction algorithm which could reconstruct particles with low velocity.

Table 1: The table shows the efficiency of FCPs passing reconstructions and restrictions in track quality and transverse momentum at different charge and mass points.

	$1/3\ e$	$1/2\ e$	$2/3\ e$
1000 GeV	$(9.66 \pm 0.17)\%$	$(43.80 \pm 0.29)\%$	$(86.46 \pm 0.20)\%$
200 GeV	$(3.20 \pm 0.10)\%$	$(18.33 \pm 0.22)\%$	$(71.34 \pm 0.26)\%$
30 GeV	$(0.42 \pm 0.04)\%$	$(7.65 \pm 0.15)\%$	$(58.68 \pm 0.28)\%$

4.4 Reconstructed transverse momentum and velocity

In the muon reconstruction, candidate particles are assumed to have a unit charge. Thus, the reconstructed p_{T} of an FCP is in principle scaled by a factor of one over the value of its charge given that $p_{\mathrm{T}} = 0.3zB\rho$, where z is the charge of the particle and ρ is the radius of the track. The reconstructed p_{T} of FCP has been drawn as a function of its truth p_{T} into profile histograms shown in Fig. 5, where those points with entries less than ten are ignored and the last bin has been extended due to the statistics power. FCPs with different masses have been drawn in colorful points while muons from Z boson decays are drawn in grey points. FCPs with higher mass possess a higher p_{T} range, which is consistent with Fig. 4(d). The reconstructed p_{T} is as expected scaled by 1 over the charge of the FCP with respect to the measurement of a muon with the same momentum. The p_{T} reconstruction has good precision in the low-p_{T} region while it becomes less precise in the high-p_{T} region.

As MuGirl fits the velocity for muon-like objects during the reconstruction, the reconstructed velocity of FCPs using this technique could be utilized in further analysis. The good performance of the velocity reconstruction is indicated in Fig. 6 where the reconstructed velocity is drawn as a function of the truth velocity.

4.5 $\mathrm{d}E/\mathrm{d}x$ variables

A heavy stable FCP will leave a very characteristic track in the ATLAS detector. Considering the fractional charge it carries, the energy deposited by an FCP in detectors will be lower than that of a muon. In addition, the deposited energy depends on the $\beta\gamma$ which equals p/m. According to the Bethe-Bloch formula, an FCP would deposit more energy than a minimum ionizing particle with the same charge, if $\beta\gamma$ of the FCP is away from three.

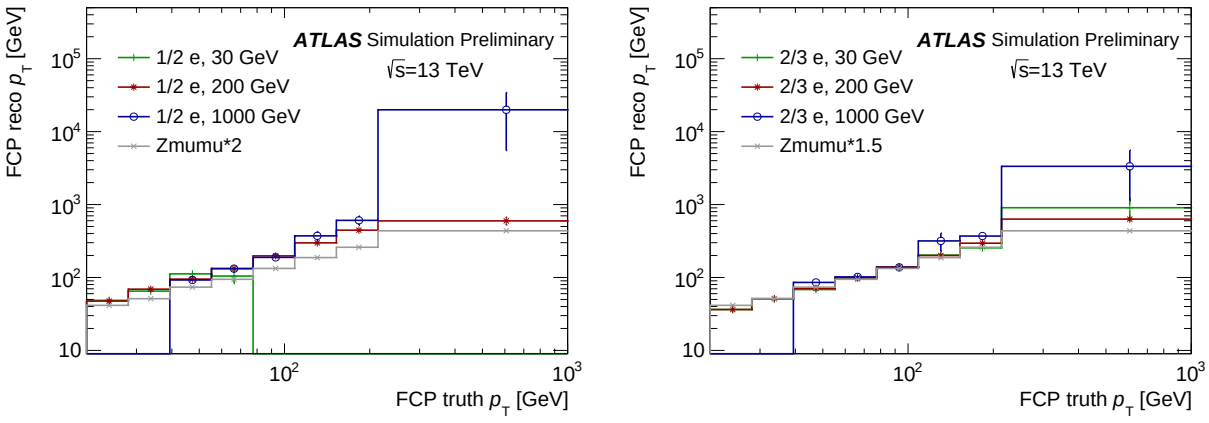

(a) (b)

Figure 5: Profile histograms of reconstructed p_{T} Vs. truth p_{T} of FCPs of different charges: (a) $2/3\ e$, (b) $1/2\ e$ as functions. In each histogram, FCPs with different masses are drawn in colorful lines, and muons decayed from Z boson are drawn in the grey line.

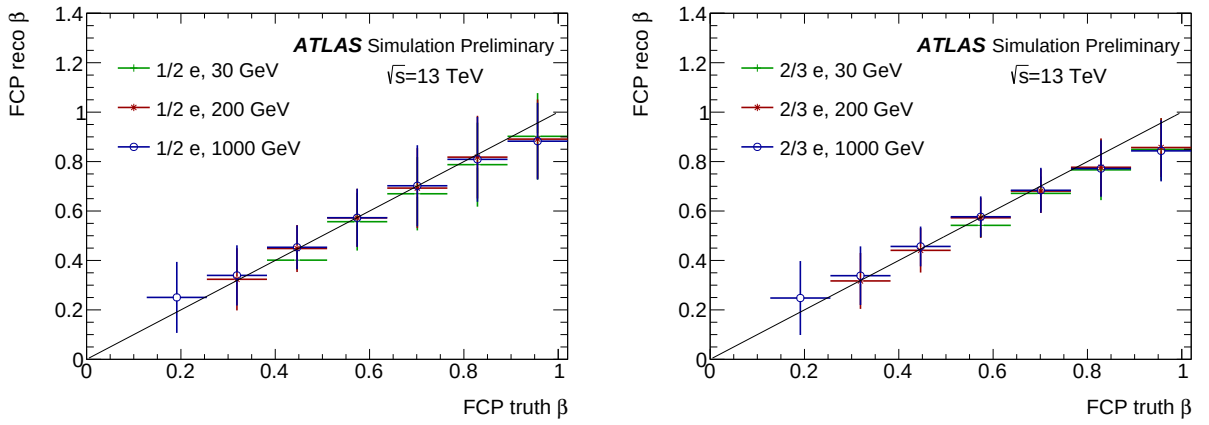

(a) (b)

Figure 6: Profile histograms of reconstructed velocity Vs. truth velocity of FCPs of different charges: (a) $2/3\ e$, (b) $1/2\ e$ as functions. An auxiliary line $y = x$ is drawn together to indicate the goodness of the reconstructed velocity.

In the ATLAS detector, the pixel, TRT, and MDT detectors offer measurements on dE/dx left by tracks of charged particles. The distributions of dE/dx of these detectors for FCPs are drawn to uncover their potential in distinguishing FCPs from muons. Muons from Z bosons decays are selected as references. The data-based calibration for dE/dx measurements is not introduced here while it could be applied in further data analysis. Since the detectors are expected to be less ionized by FCPs, the efficiency of dE/dx variable is considered as well. Thirty thousand events are generated and analyzed for FCPs of each charge and mass point.

4.5.1 Pixel dE/dx

The pixel detectors use the time-over-threshold (ToT) method to measure the charge ionized by the charged particle. The ionization loss per unit length (dE/dx) of the incoming charged particle is measured, calculating the truncated mean of the dE/dx of all hits associated with the track of the particle [26]. The pixel dE/dx is additionally restricted to be associated with a track which has at least one valid dE/dx measurement in the pixel detectors.

The pixel dE/dx left by $1/2$ e and $2/3$ e FCPs of different mass points are shown in Fig. 7, as well as Zmumu ($Z \rightarrow \mu\mu$) events. The average pixel dE/dx is roughly quadratically correlated with the charge of FCPs, as expected. While comparing FCPs with the same charge and different masses, heavier FCPs gain some enhancements in pixel dE/dx due to the $\beta\gamma$ tuning and the tails get longer for the lower propagating velocity of massive FCPs. The fraction of tracks with a valid pixel dE/dx is 100% since the reconstruction of objects is required to have at least one valid dE/dx measurement in the pixels.

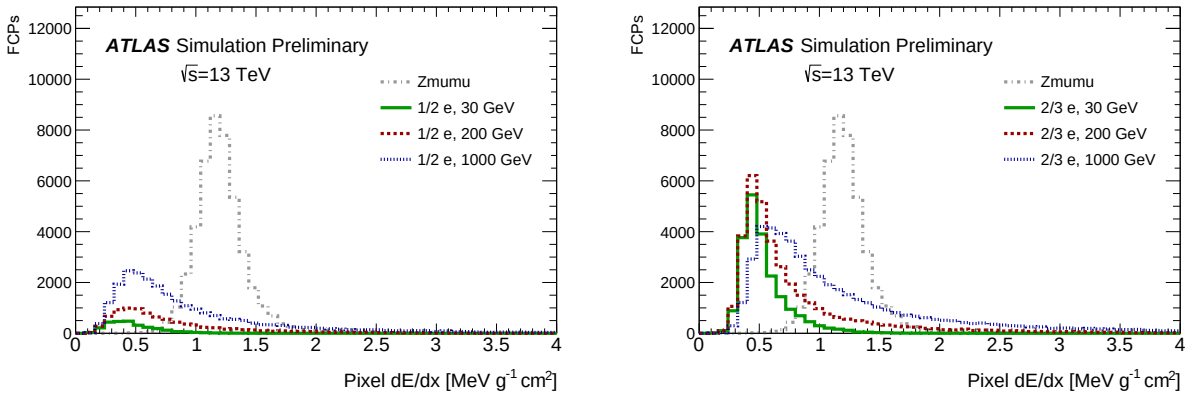

(a) (b)

Figure 7: Histograms of pixel dE/dx of FCPs of different charges: (a) $1/2$ e, (b) $2/3$ e. In each histogram, FCPs with different masses are drawn in colorful lines, and muons decayed from Z boson are drawn in the grey line.

4.5.2 TRT dE/dx

TRT detectors construct an estimator for dE/dx using the ToT-based method, with ToT defined as the longest time above the low threshold which is used to identify the energy deposition. The TRT dE/dx is defined as the truncated average of ToT of all hits [27] and its unit is ns/mm.

The TRT dE/dx for FCPs at different charge and mass points are shown in Fig. 8(a) and Fig. 8(b), with Zmumu events as reference. The dE/dx of TRT detectors is related to the charge and mass of FCP. The summary of the relative efficiency, which is defined as the ratio between number of tracks with a valid TRT dE/dx measurement and number of all tracks with event selection requirements, for FCP is shown in Table 2. The inefficiency of TRT dE/dx is partially related to the unused hits with low quality, such as the saturated hits.

Table 2: The table containing the rate of the FCPs featuring a valid TRT dE/dx for different charge and mass points.

	$1/3\ e$	$1/2\ e$	$2/3\ e$
1000 GeV	$(48.6 \pm 0.9)\%$	$(75.8 \pm 0.4)\%$	$(86.98 \pm 0.21)\%$
200 GeV	$(48.8 \pm 1.6)\%$	$(73.9 \pm 0.6)\%$	$(76.51 \pm 0.29)\%$
30 GeV	$(51.63 \pm 1.41)\%$	$(68.52 \pm 1.00)\%$	$(71.35 \pm 0.34)\%$

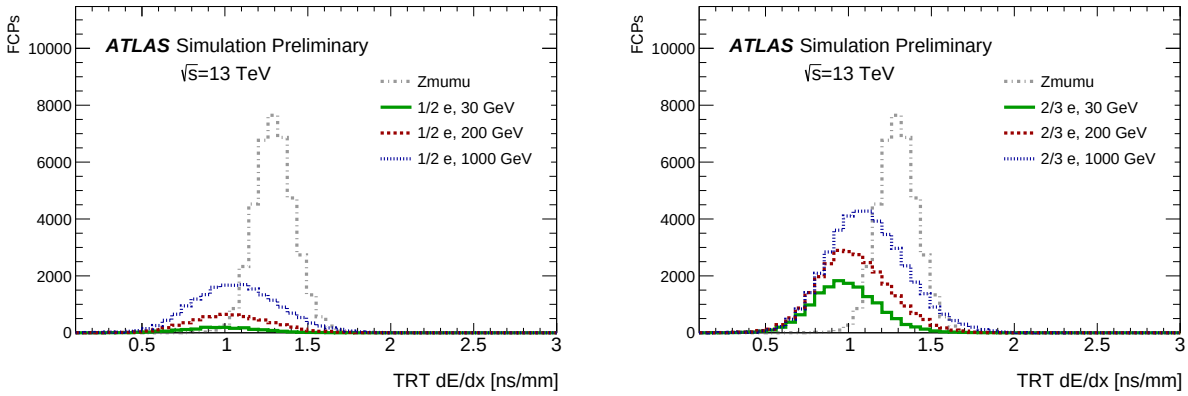

(a) (b)

Figure 8: Histograms of TRT dE/dx for FCPs of different charges: (a) $1/2\ e$, (b) $2/3\ e$. In each histogram, FCPs with different masses are drawn in colorful lines, and muons decayed from Z boson are drawn in the grey line.

4.5.3 MDT dE/dx

Each drift tube of the MDT system provides a signal proportional to the ionization charge, which is then converted by an analog-digital-converter. The mean digital counts of one track are used to estimate dE/dx embedded in the simulation framework. The distribution of MDT dE/dx, shown in Fig. 9, is found to be closer to zero for particles carrying unit charge.

In Table 3 which summarizes the ratio between the number of tracks with a valid MDT dE/dx and number of all tracks with event selection requirements, it is found that MDT detectors feature a high reconstruction rate of dE/dx for FCPs reconstructed and passed selections. The different number and quality of hits used in track and dE/dx reconstruction result in inefficiency.

Table 3: The table containing the rate of the FCP featuring with a valid MDT dE/dx for different charge and mass points.

	$1/3\ e$	$1/2\ e$	$2/3\ e$
1000 GeV	$(97.44 \pm 0.29)\%$	$(96.90 \pm 0.15)\%$	$(97.95 \pm 0.09)\%$
200 GeV	$(98.1 \pm 0.4)\%$	$(95.87 \pm 0.27)\%$	$(96.40 \pm 0.13)\%$
30 GeV	$(98.47 \pm 0.35)\%$	$(97.54 \pm 0.32)\%$	$(96.80 \pm 0.13)\%$

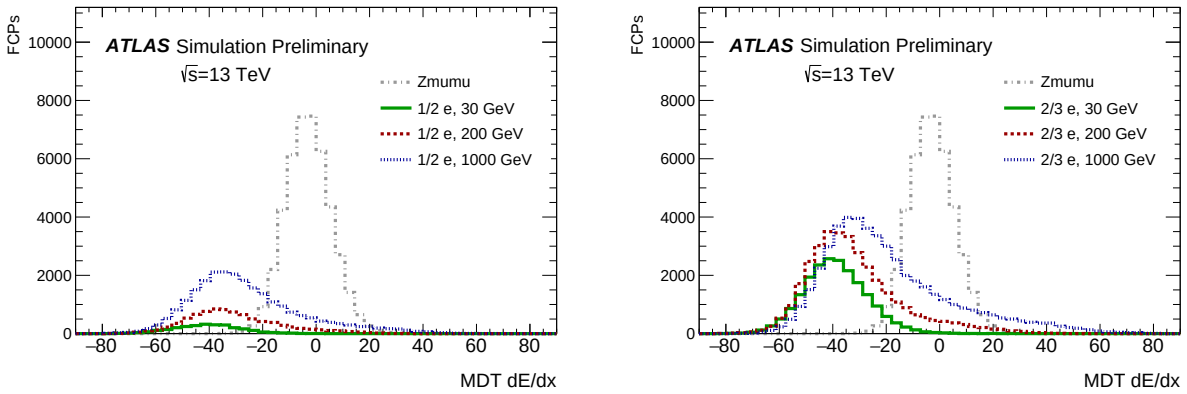

(a) (b)

Figure 9: Histograms of MDT dE/dx of FCPs of different charges: (a) $1/2\ e$, (b) $2/3\ e$. In each histogram, FCPs with different masses are drawn in colorful lines, and muons decayed from Z boson are drawn in the grey line.

4.6 Trigger efficiency

Interesting events are accepted by the trigger system which consists of Level-1 (L1) [28] trigger and High Level Trigger (HLT) [29]. The Level-1 trigger system is implemented in custom-built electronics. It is the first stage of the trigger, and responsible for reducing the initial 40 MHz rate to less than 100 kHz. HLT is implemented in software executed on large computing farms and reduces the trigger rate to approximately 1 kHz.

FCPs deposit less energy in the detectors than the SM particles carrying unit charge. The trigger efficiency of FCPs is also lower. The effect of the abnormal charge in RPC and TGC is included in the ATLAS simulation and digitization process. But for FCPs with different charges and masses, both the L1 trigger and HLT are studied extensively.

4.6.1 Level 1 trigger

The L1 muon triggers are studied since the performance of FCPs is expected to be similar to the one of the muons. They can operate with various p_{T} thresholds, the label of each coincidence being "L1_MU" + the transverse momentum threshold. The L1 trigger is based on hit coincidences in the RPC and TGC detectors, in the barrel and in the endcaps respectively. If the trigger is fired, the η, ϕ and p_{T} threshold of the region of interest (ROI) will be written in the event data. The particle that fires the trigger could be found by matching the reconstructed FCP candidates with a ROI. If the ΔR between the FCP and the

ROI is lower than 0.1, this FCP is selected to be the one that fired the trigger. To make sure the FCPs hit the RPC or TGC with enough energy, additional phase space cuts are required. For RPC, the range of FCPs pseudorapidity should be 0.1 to 1.05 and the p_{T} should be larger than 20 GeV at the generator level. Limited by the cuts of phase space, only part of total FCPs could be selected. Gaps in coverage due to services or disabled detector regions (insensitive regions) will contribute to the inefficient events. The efficiency is defined as the ratio between FCPs matched to a trigger ROI in events where the trigger has fired, and all events with an FCP in the fiducial region. The L1 efficiency of FCPs with mass 30 GeV and different charges are shown in Fig. 10(a). As the charge decreases, the efficiency drops. Since one additional RPC layer is included in the coincidence algorithm from L1_MU10 to L1_MU11, the efficiency declined sharply here. The similar result of FCPs with charge $2/3\ e$ and different masses are shown in Fig. 10(b). The overall efficiency for the low-p_{T} thresholds of the muon barrel L1 of FCPs is summarized in Table 4. As a comparison, the RPC efficiency of muons with the same algorithm is shown in Fig. 10(c). The overall efficiency of muons is $82.8 \pm 0.1\%$.

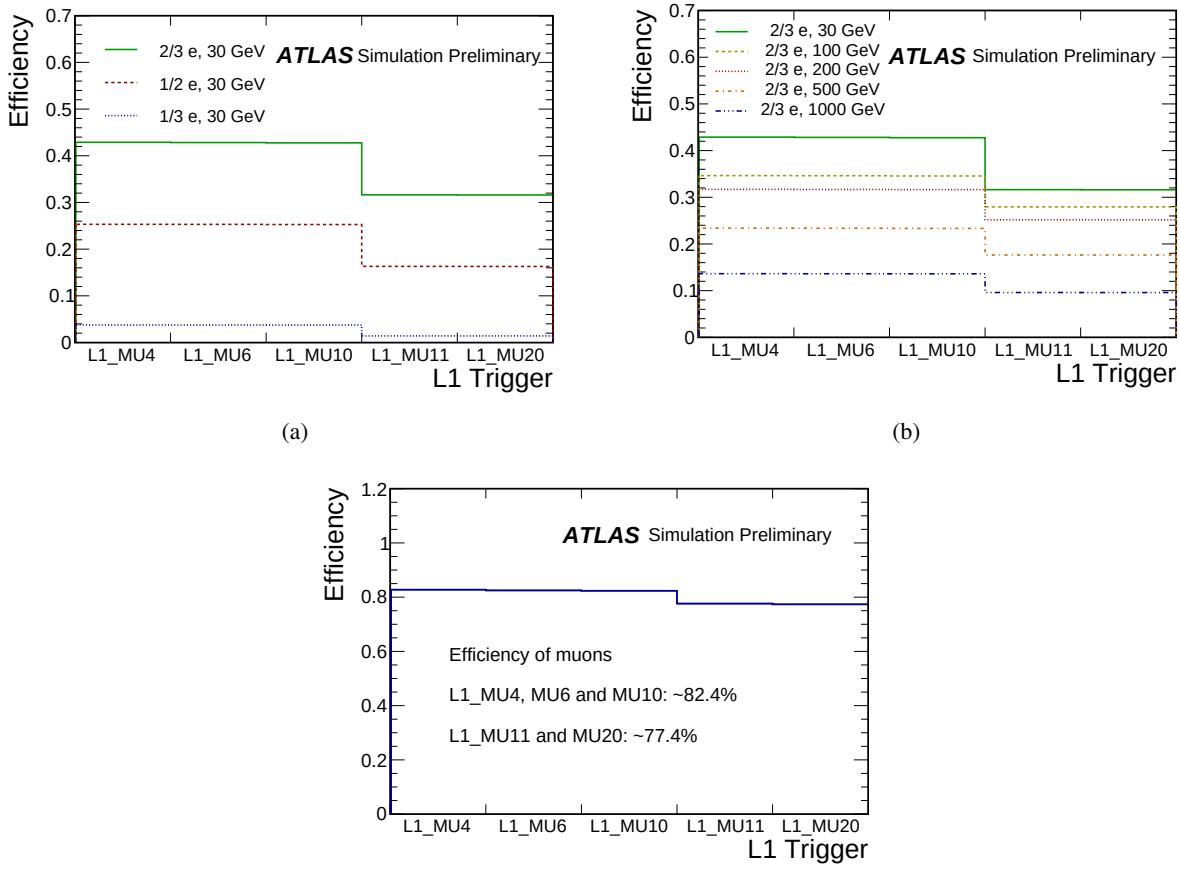

Figure 10: Efficiency of particles with different charges (a) and different masses (b) passing L1 trigger in RPC phase space. Efficiency of muons (c) is shown as a comparison.

For TGC, the range of FCPs pseudorapidity should be 1.05 to 2.40, and the p_{T} should be larger than 20 GeV at the generator level. The efficiency of particles with mass 30 GeV and different charges is shown in Fig. 11(a). Limited by the high threshold applied to electronic signals of TGC, the efficiency of FCPs in

Table 4: RPC L1 trigger efficiency (overall or lowest p_T) of FCPs with different masses and charges.

	$1/3\ e$	$1/2\ e$	$2/3\ e$
1000 GeV	$(1.36 \pm 0.07)\%$	$(8.65 \pm 0.17)\%$	$(13.64 \pm 0.21)\%$
200 GeV	$(2.43 \pm 0.12)\%$	$(17.73 \pm 0.29)\%$	$(31.7 \pm 0.4)\%$
100 GeV	$(2.70 \pm 0.14)\%$	$(19.55 \pm 0.34)\%$	$(34.6 \pm 0.4)\%$
30 GeV	$(3.754 \pm 0.097)\%$	$(25.3 \pm 0.5)\%$	$(42.9 \pm 0.5)\%$

TGC is quite lower. During the digitization of TGC, energy deposition and threshold are tuned precisely to ensure the equal of efficiency between data and MC [30]. For particles with small charge, the induced signals tend to fail the TGC threshold. Same as RPC, the insensitive regions of endcap will also contribute to the inefficient events. The results of FCPs with charge $2/3\ e$ and different masses are shown in Fig. 11(b). The efficiency of FCPs with charge $2/3\ e$ is lower than 5% while that of the other two charge points are almost zero. This indicates that for FCPs with charge $1/2\ e$ and $1/3\ e$, TGC is hard to be used in the FCP searching. As a comparison, the TGC efficiency of muons is shown in Fig. 11(c). The efficiency of muon is $95.6 \pm 0.1\%$.

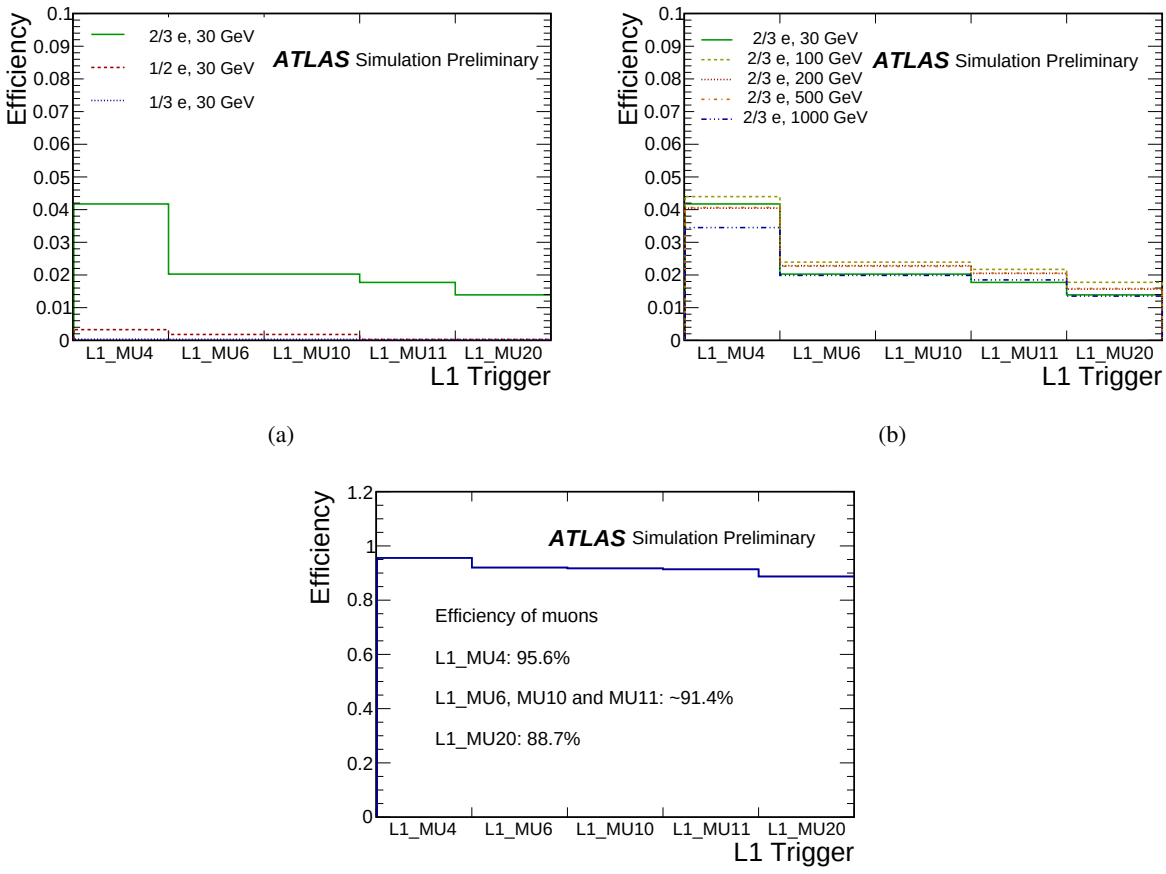

Figure 11: Efficiency of particles with different charges (a) and different masses (b) passing L1 trigger in TGC phase space. Efficiency of muons (c) is shown as a comparison.

4.6.2 High level trigger

The HLT efficiency is studied at event level. Besides the L1 seed of HLTs, no requirement of additional L1 trigger is applied in this study. According to the preliminary study, the FCP events are only sensitive to five high-level triggers, including two single muon triggers (HLT_mu50 and HLT_mu26_ivarmedium), two late muon triggers (HLT_mu10_mgonly_L1LATE-MU10_J50 and HLT_mu10_mgonly_L1LATE-MU10_XE40) and one jet trigger (HLT_j420). The requirements of HLT are described in Table 5. The two late muon triggers [31] are the designed specifically for massive long-lived particles. These two triggers are originated from level 1 triggers requiring a 50 GeV jet (L1_J50) or 40 GeV of missing transverse momentum (L1_XE40). When these two level 1 triggers are fired, the algorithm will search for the hits of innermost and outermost RPCs in the next Bunch-Crossing (BC). Once the hits of innermost and outermost RPCs are located at the same BC, this high level trigger will be fired. This will be helpful especially for particles with β from 0.5 to 0.7. Considering the low efficiency of TGC, only the HLT efficiency of RPC is measured. FCPs with transverse momentum larger than 25 GeV and pseudorapidity between 0.1 and 1.05 could be selected as "good" objects. Events with at least one "good" object are recorded as "Events in ROI" which is normalized to 1 in the histograms shown in Fig. 12. The event number which scaled to fraction of "Events in ROI" are the efficiency of triggers. FCP events with mass 30 GeV and different charges are drawn in Fig. 12(a). The efficiency of 30 GeV FCPs with $2/3$ e dropped to about 22% while for muons it is around 91%. In the low mass region, the most sensitive triggers are the two single muon triggers. The efficiency with charge $2/3$ e and different masses are drawn in Fig. 12(c). When the mass of FCPs gets higher, the jet trigger and two late muon triggers tend to work since the behaviour is similar to the one of a muon with a very low velocity and the p_{T} of the backward jet increases to a high level. And as shown in Fig. 12(b), events in charge points $1/3$ e and $1/2$ e could also pass these three additional triggers. Since the events fired by HLT_mu10_mgonly_L1LATE-MU10_J50 are fully overlapped with HLT_mu10_mgonly_L1LATE-MU10_XE40, the first late muon trigger could be removed in the final trigger list. Thus HLT_mu50, HLT_mu26_ivarmedium, HLT_mu10_mgonly_L1LATE-MU10_XE40 and HLT_j420 are finally chosen. All the efficiency results of the combined trigger are summarized in Table 6. Benefitting from the later muon triggers, the efficiencies of FCPs with mass 1000 GeV are improved.

Table 5: Detailed requirements of different HLTs.

	Requirements
HLT_mu50	at least one muon with $p_{\mathrm{T}} > 50$ GeV
HLT_mu26_ivarmedium	at least one muon with $p_{\mathrm{T}} > 26$ GeV and isolation "medium"
HLT_mu10_mgonly_L1LATE-MU10_J50	at least one MuGirl muon with $p_{\mathrm{T}} > 10$ GeV in the next bunch crossing of L1_J50 (L1 trigger with requirement p_{T} of one jet > 50 GeV)
HLT_mu10_mgonly_L1LATE-MU10_XE40	at least one MuGirl muon with $p_{\mathrm{T}} > 10$ GeV in the next bunch crossing of L1_XE40 (L1 trigger with requirement p_{T} of $E_{\mathrm{T}}^{\mathrm{miss}}$ > 40 GeV)
HLT_j420	at least one jet with $p_{\mathrm{T}} > 420$ GeV

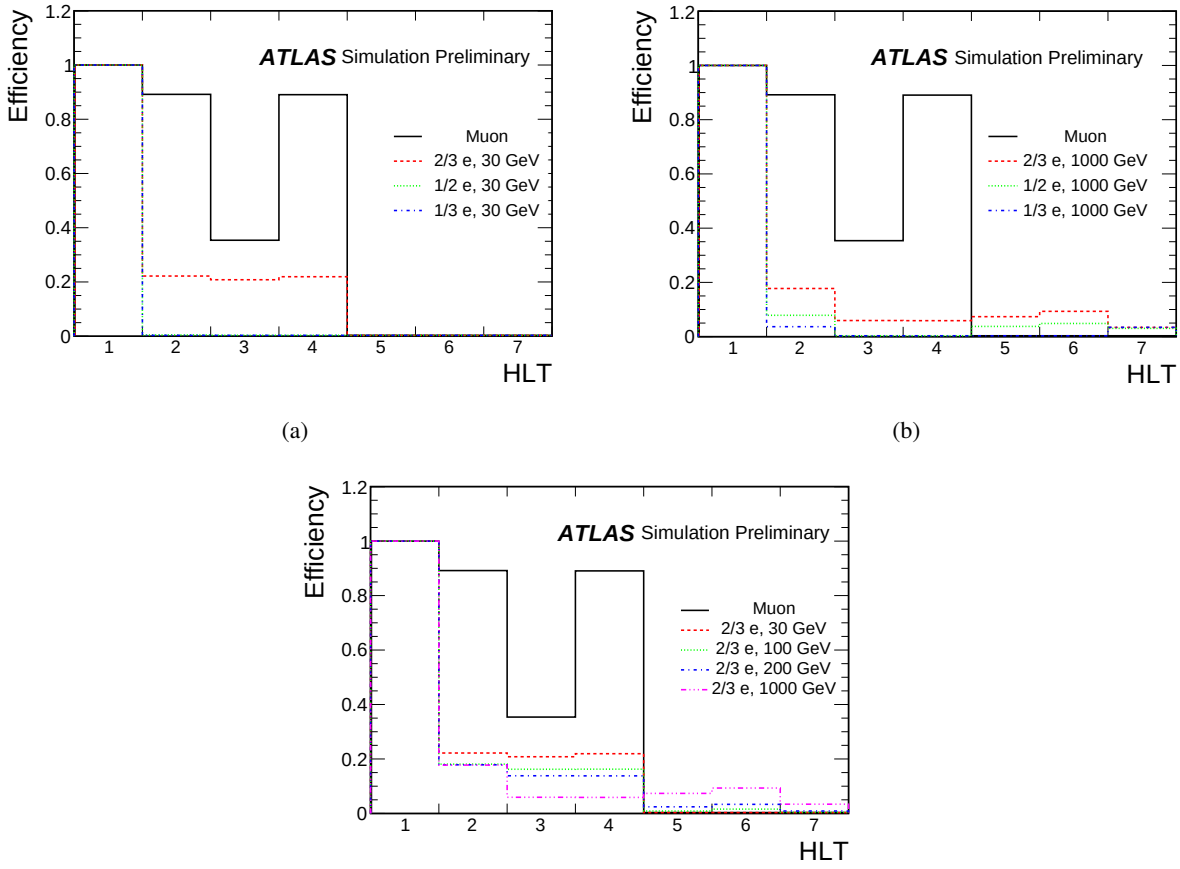

Figure 12: Efficiency of events with different charges and mass 30 GeV (a), different charges and mass 1000 GeV (b) and different masses and charge $2/3\ e$ (c) passing HLT trigger in RPC phase space. Labels of x-axis: 1: Event in ROI; 2: Combined Trigger; 3: HLT_mu50; 4: HLT_mu26_ivarmedium; 5: HLT_mu10_mgonly_L1LATE-MU10_J50; 6: HLT_mu10_mgonly_L1LATE-MU10_XE40; 7: HLT_j420.

Table 6: Combined HLT efficiency of FCPs with different masses and charges.

	$1/3\ e$	$1/2\ e$	$2/3\ e$
1000 GeV	$(3.66 \pm 0.13)\%$	$(7.86 \pm 0.19)\%$	$(17.75 \pm 0.27)\%$
200 GeV	$(0.88 \pm 0.08)\%$	$(2.57 \pm 0.26)\%$	$(17.86 \pm 0.34)\%$
100 GeV	$(0.22 \pm 0.05)\%$	$(0.93 \pm 0.09)\%$	$(18.1 \pm 0.4)\%$
30 GeV	$(0.018 \pm 0.006)\%$	$(0.48 \pm 0.09)\%$	$(22.2 \pm 0.5)\%$

4.7 Final efficiency

Among the 30k events in every MC sample with different charges and masses, 60k FCPs are generated. With the selection of detector acceptance ($|\eta| < 2.5$ and $p_{\mathrm{T}} > 27$ GeV in reconstruction level), triggers (logical OR for all the HLTs in Section 4.6.2) and ATLAS reconstruction (standard muon and MuGirl reconstruction algorithm with track requirements), only part of them could be reconstructed. Besides, no requirement of dE/dx is applied. The ratio of the final reconstructed particles and all the original truth FCPs is defined as the final efficiency. The final efficiency is associated with the charge and mass, and summarized in Table 7. The efficiencies for charge $1/2\ e$ and $2/3\ e$ are quite low, but there are still some FCPs that could be triggered and reconstructed. For the charge point $1/3\ e$, nearly zero reconstructed objects could be selected.

Table 7: Final efficiency of FCPs with different masses and charges.

	$1/3\ e$	$1/2\ e$	$2/3\ e$
1000 GeV	$(0.160 \pm 0.016)\%$	$(4.47 \pm 0.08)\%$	$(14.22 \pm 0.14)\%$
200 GeV	$(0.0050 \pm 0.0029)\%$	$(0.635 \pm 0.032)\%$	$(7.00 \pm 0.10)\%$
100 GeV	$(0.0033 \pm 0.0024)\%$	$(0.094 \pm 0.011)\%$	$(8.72 \pm 0.12)\%$
30 GeV	$(0.00 + 3.07e - 3)\%$	$(0.075 \pm 0.011)\%$	$(3.86 \pm 0.07)\%$

5 Conclusion

This note presents the simulated detector performance of FCPs with long lifetimes. FCPs are reconstructed to be muon-like particles as they are assumed to be very heavy and participate only in EM and weak interactions. The detector performance has been studied based on MC simulation including the L1 and HLT triggers, the energy deposition in pixel, TRT and MDT detectors and the reconstructed transverse momentum. Due to the smaller charge, FCPs deposit less energy in detectors. Correlated with the energy deposition, the trigger efficiencies are lower. The reconstructed transverse momentum is larger than that of the unit charged particles by a factor of approximately 1/|Q|.

The simulation results show that the reconstructed energy deposition in pixel, TRT and MDT are the sensitive parameters to distinguish FCPs from the background muons and will be key variables to utilize in the future searches for FCPs with collision data in the ATLAS experiment.

References

[1] ATLAS Collaboration, *Observation of a new particle in the search for the Standard Model Higgs boson with the ATLAS detector at the LHC*, Physics Letters B **716** (2012) 1 (cit. on p. 2).

[2] CMS Collaboration, *Observation of a new boson at a mass of 125 GeV with the CMS experiment at the LHC*, Physics Letters B **716** (2012) 30 (cit. on p. 2).

[3] R. Slansky et al., *Observable Fractional Electric Charge in Broken Quantum Chromodynamics*, Phys. Rev. Lett. **47** (1981) 887 (cit. on p. 2).

[4] B. Acharya et al., *Search for magnetic monopoles produced via the Schwinger mechanism*, Nature **602** (2022) 63, URL: https://doi.org/10.1038/s41586-021-04298-1 (cit. on p. 2).

[5] I. E. Gulamov, E. Y. Nugaev and M. N. Smolyakov, *Analytic Q-ball solutions and their stability in a piecewise parabolic potential*, Phys. Rev. D **87** (8 2013) 085043, URL: https://link.aps.org/doi/10.1103/PhysRevD.87.085043 (cit. on p. 2).

[6] Martin L. Perl, Eric R. Lee and Dinesh Loomba, *Searches for Fractionally Charged Particles*, Annual Review of Nuclear and Particle Science **59** (2009) 47 (cit. on p. 2).

[7] CMS Collaboration, *Searches for long-lived charged particles in pp collisions at $\sqrt{s} = 7$ and 8 TeV*, JHEP **07** (2013) 122, arXiv: 1305.0491 [hep-ex] (cit. on p. 2).

[8] CMS Collaboration, *Search for fractionally charged particles in pp collisions at $\sqrt{s} = 13$ TeV*, CMS-PAS-EXO-19-006, 2022, URL: https://cds.cern.ch/record/2841994 (cit. on p. 2).

[9] ATLAS Collaboration, *Search for heavy long-lived multi-charged particles in the full Run-II pp collision data at $\sqrt{s} = 13$ TeV using the ATLAS detector*, ATLAS-CONF-2022-034, 2022, URL: https://cds.cern.ch/record/2810156 (cit. on p. 2).

[10] ATLAS Collaboration, *Search for heavy, long-lived, charged particles with large ionisation energy loss in pp collisions at sqrts = 13TeV using the ATLAS experiment and the full Run 2 dataset*, (2022), arXiv: 2205.06013 [hep-ex] (cit. on p. 2).

[11] ATLAS Collaboration, *Search for heavy long-lived multi-charged particles in proton-proton collisions at $\sqrt{s} = 13$ TeV using the ATLAS detector*, Phys. Rev. D **99** (2019) 052003 (cit. on p. 2).

[12] H. Bethe, *Zur Theorie des Durchgangs schneller Korpuskularstrahlen durch Materie*, Annalen der Physik **397** (1930) 325 (cit. on p. 2).

[13] ATLAS Collaboration, *The ATLAS Experiment at the CERN Large Hadron Collider*, Journal of Instrumentation **3** (2008) S08003 (cit. on p. 3).

[14] ATLAS Collaboration, *ATLAS software and firmware*, ATLAS twiki (2021), URL: https://twiki.cern.ch/twiki/bin/view/AtlasProtected/PubComCommonText#ATLAS_software_and_firmware (cit. on p. 3).

[15] A. Miucci, *The ATLAS Insertable B-Layer project*, Journal of Instrumentation **9** (2014) C02018, URL: https://doi.org/10.1088/1748-0221/9/02/c02018 (cit. on p. 3).

[16] J. Alwall, M. Herquet, F. Maltoni, O. Mattelaer and T. Stelzer, *MadGraph 5 : Going Beyond*, JHEP **06** (2011) 128, arXiv: 1106.0522 [hep-ph] (cit. on p. 4).

[17] A. Buckley et al., *LHAPDF6: parton density access in the LHC precision era*, The European Physical Journal C **75** (2015), URL: https://doi.org/10.1140%2Fepjc%2Fs10052-015-3318-8 (cit. on p. 4).

[18] T. Sjöstrand et al., *An introduction to PYTHIA 8.2*, Computer Physics Communications **191** (2015) 159, ISSN: 0010-4655, URL: https://www.sciencedirect.com/science/article/pii/S0010465515000442 (cit. on p. 4).

[19] ATLAS Collaboration, *The ATLAS Simulation Infrastructure*, Eur. Phys. J. C **70** (2010) 823 (cit. on p. 8).

[20] S. Agostinelli et al., *GEANT4–a simulation toolkit*, Nucl. Instrum. Meth. A **506** (2003) 250 (cit. on p. 8).

[21] ATLAS Collaboration, *Muon reconstruction performance of the ATLAS detector in proton–proton collision data at* $\sqrt{s} = 13$ *TeV*, Eur. Phys. J. C **76** (2016) 292, arXiv: 1603.05598 [hep-ex] (cit. on p. 8).

[22] S. Tarem, Z. Tarem, N. Panikashvili and O. Belkind, *MuGirl – Muon identification in the ATLAS detector from the inside out*, IEEE Transactions on Nuclear Science **1** (2006) 617 (cit. on p. 8).

[23] ATLAS Collaboration, *Muon reconstruction efficiency in reprocessed 2010 LHC proton–proton collision data recorded with the ATLAS detector*, ATLAS-CONF-2011-063, 2011, URL: https://cds.cern.ch/record/1345743 (cit. on p. 8).

[24] S. Tarem and A. Collaboration, *Reconstruction And Identification Of Heavy Long-Lived Particles At The ATLAS Detector At The LHC*, AIP Conference Proceedings **1200** (2010) 762 (cit. on p. 8).

[25] Tarem, S., Bressler, S., Nomoto, H. and Di Mattia, A., *Trigger and reconstruction for heavy long-lived charged particles with the ATLAS detector*, Eur. Phys. J. C **62** (2009) 281 (cit. on p. 8).

[26] ATLAS Collaboration, *dE/dx measurement in the ATLAS Pixel Detector and its use for particle identification*, ATLAS-CONF-2011-016, 2011, URL: https://cds.cern.ch/record/1336519 (cit. on p. 11).

[27] ATLAS Collaboration, *Particle Identification Performance of the ATLAS Transition Radiation Tracker*, ATLAS-CONF-2011-128, 2011, URL: https://cds.cern.ch/record/1383793 (cit. on p. 11).

[28] W. Buttinger, *The ATLAS Level-1 Trigger System*, Journal of Physics: Conference Series **396** (2012) 012010, URL: https://doi.org/10.1088/1742-6596/396/1/012010 (cit. on p. 13).

[29] C. Gabaldon, *Performance of the ATLAS Trigger System*, Journal of Instrumentation **7** (2012) C01092, URL: https://doi.org/10.1088/1748-0221/7/01/c01092 (cit. on p. 13).

[30] ATLAS Collaboration, *Geant4 Muon Digitization in the ATHENA Framework*, ATL-SOFT-PUB-2007-001, 2007, URL: https://cds.cern.ch/record/1010495 (cit. on p. 15).

[31] J. J. Heinrich, 'Search for charged stable massive particles with the ATLAS detector', 2018, URL: http://nbn-resolving.de/urn:nbn:de:bvb:19-221830 (cit. on p. 16).